Nonadiabatic dynamics in the photodissociation of ICH$_2$CN at 266 and 304 nm studied by the velocity map imaging

Kyoung-Seok Lee, Jung-Sik Lim, Doo Sik Ahn, Kyo-Won Choi, and Sang Kyu Kim[a)]
Department of Chemistry and School of Molecular Science (BK21), Korea Advanced Institute of Science and Technology (KAIST), Daejeon 305-701, Republic of Korea

Young S. Choi
Department of Chemistry, Inha University, Inchon 402-751, Republic of Korea

Photodissociation dynamics of iodoacetonitrile (ICH$_2$CN) have been investigated at pump wavelengths of 266 and 304 nm using a photofragment ion image velocity mapping technique. At both wavelengths, the prompt C–I bond rupture takes place on the repulsive excited states to give $I(^2P_{3/2})$ and $I^*(^2P_{1/2})$, and their speed and spatial distributions are simultaneously measured. The recoil anisotropy parameter (β) at 266 nm is determined to be 1.10 and 1.60 for I and I^*, respectively, while it is found to be much higher at 304 nm to give β=1.70 and 1.90 for I and I^*, respectively. The branching ratios for I^*/I channels are measured to be 0.724 and 0.136 at 266 and 304 nm, respectively, giving insights on nonadiabatic transition phenomena and relative oscillator strengths of optically accessible transitions of ICH$_2$CN. Accordingly, relative oscillator strengths of parallel/perpendicular transitions and nonadiabatic transitions among the excited states are quantitatively characterized. A large portion of the available energy (41%–48%) goes into the internal energy of the CH$_2$CN fragment. A modified impulsive model in which the CH$_2$CN fragment is assumed to be rigid predicts the energy disposal quite well. Delocalization of an unpaired electron of the CH$_2$CN radical during the C–I bond cleavage, leading to a large structural change of the CH$_2$CN moiety, may be responsible for internally hot fragments. © *2006 American Institute of Physics*. [DOI: 10.1063/1.2167748]

I. INTRODUCTION

Photodissociation dynamics of alkyl halides have been both extensively and intensively studied for several decades since they provide the prototypical system not only of direct-bond dissociations on repulsive electronic states but also of intriguing nonadiabatic transitions along the reaction coordinates.[1–13] For instance, it is now well known that the *A* band of CH$_3$I in the UV region is the $\sigma^*(C-I) \leftarrow n(I)$ transition and it is associated with three repulsive electronic excited states: $^3Q_1(2E)$, $^3Q_0(2A_1)$, and $^1Q_1(3E)$ in Mulliken's notations.[14,15] Transition dipole moment is parallel to the dissociating C–I bond for the $^3Q_0(2A_1)$ transition, while it is perpendicular to the C–I bond axis for transitions to $^3Q_1(2E)$ and $^1Q_1(3E)$. The absorption is followed by a direct C–I bond dissociation along the reaction coordinate where the Landau-Zener-type nonadiabatic transitions take place between $^3Q_0(2A_1)$ and $^1Q_1(3E)$ states. Namely, though a wave packet initially prepared on the $^3Q_0$ state is adiabatically correlated to $I(^2P_{3/2})$+CH$_3$ fragments, because of the nonadiabatic interaction with an upper lying $^1Q_1$ state, it has a significant probability to go to $I^*(^2P_{1/2})$+CH$_3$ fragments at the asymptotic limit. A number of experimental and theoretical works have been carried out to gain deep insights on relative oscillator strengths of these mixed transitions,

detailed multidimensional dynamics, and nonadiabatic transition probabilities along the C–I bond elongation of CH$_3$I.[1,2,5–7,10,13,15–27] Photodissociation dynamics of many other alkyl or aryl halides have also been investigated in many laboratories, giving the nature of the C–I bond rupture dependent on different chemical environments.[1,2,5–7,10,16,17,19–22,24–26,28] In particular, the recent development of the velocity-mapped ion imaging method, with which speed and angular distributions of photofragments are simultaneously measured with great accuracies, has stimulated a lot of recent important studies on laser-induced bond dissociation dynamics in many interesting chemical systems.[27,29–31]

Here, we report photodissociation dynamics of iodoacetonitrile (ICH$_2$CN) using a velocity-mapped ion imaging technique. Photodissociation of ICH$_2$CN has little been studied, while it can be a useful source for the generation of the energetic CH$_2$CN radical.[32] The presence of electron-withdrawing CN group causes a large spectral red-shift of the $\sigma^*(C-I) \leftarrow n(I)$ transition, and thus electronic transitions and electronic state couplings in ICH$_2$CN are expected to be quite different from those of CH$_3$I. In addition, since ICH$_2$CN belongs to C_s, degeneracies of the $^1Q_1$ and $^3Q_1$ states in C_{3v} are broken into their homomorphic $(4A', 2A'')$ and $(2A', 1A'')$ states, respectively, while the $^3Q_0$ state in C_{3v} is correlated to the $3A'$ state in C_s. This may give the opportunity for disentangling complex coupling dynamics among five excited states in the C_s symmetry molecule. In this work,

[a)]Author to whom correspondence should be addressed. Electronic mail:
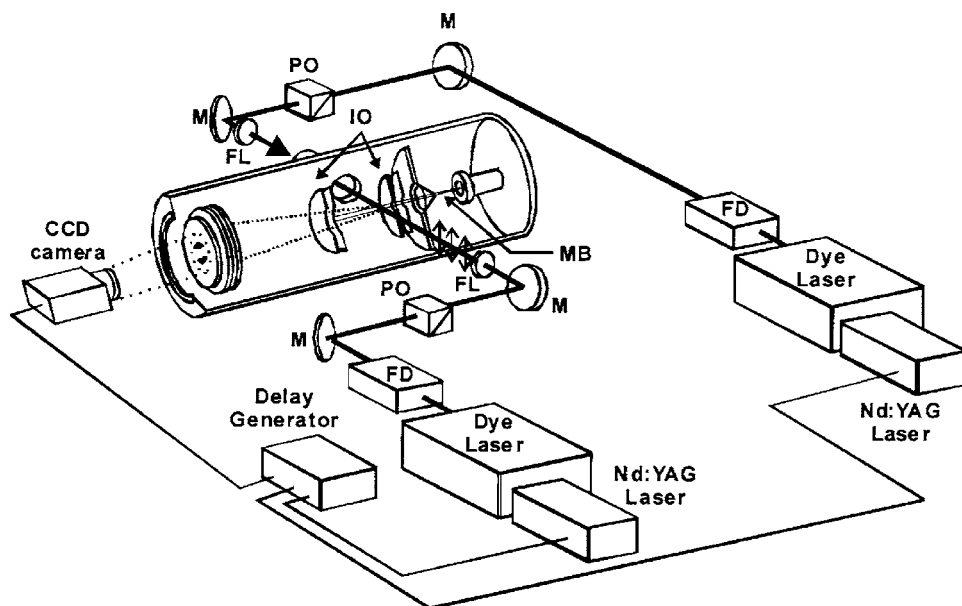sangkyukim@kaist.ac.kr

124, 124307-1

FIG. 1. Schematic diagram of the experimental setup. M: mirror, FL: focusing lens, PO: polarizing optics, IO: ion optics, FD: homemade autophase matching apparatus for frequency doubling, MB: molecular beam, and PSD: position sensitive detector.

we have measured the speed and spatial distributions of I and I^* at two different pump wavelengths of 266 and 304 nm. Also, the I^*/I branching ratios at both wavelengths are experimentally measured to give quantitative information about the relative oscillator strengths and couplings of excited states associated with the C–I bond cleavage of ICH_2CN. This work will give the deeper insight on the nature of the C–I bond cleavage in the presence of neighboring electron-withdrawing chemical moiety.

II. EXPERIMENT

Our velocity mapping apparatus consisted of a supersonic molecular beam source, a time-of-flight (TOF) mass spectrometer, and a position sensitive detector (Fig. 1). A differentially pumped vacuum chamber was equipped with two turbomolecular pumps (Varian, TV-551) to maintain the background pressure of $\sim 10^{-8}$ Torr in the ionization/detection region. A supersonic jet of the molecule was generated by expanding the gas mixture of ICH_2CN and He through a nozzle orifice (General Valve, 0.5 mm diameter) into vacuum with a backing pressure of 2 atm. The molecular beam was then skimmed through a 1 mm diam skimmer before entering the ionization chamber. Third harmonic output of a pulsed Nd:YAG (yttrium aluminum garnet) laser (Spectra Physics GCR-150) was used to pump a dye laser (Lambda-Physik Scanmate 2) to generate, after frequency doubling, laser pulses at 304.67 or 304.03 nm, which is used for probing $I(^2P_{3/2})$ or $I^*(^2P_{1/2})$ via $(2+1)$ resonant ionization using $6p[3]_{5/2}$ and $6p[1]_{1/2}$ levels, respectively. In this case, the same laser pulse was also used for pumping the parent molecule. The fourth harmonic output of another Nd:YAG laser (Coherent, Infinity) was used for the excitation of ICH_2CN at 266 nm. The laser polarization was set to be vertical to the detection axis which is defined along the time-of-flight path. A half lambda wave plate was used for the manipulation of the laser polarization. The laser was focused onto the center of the molecular beam through a planoconvex lens with a nominal focal length of 150 mm.

Ions generated by the laser irradiation were repelled, accelerated, drifted along the field-free region, and detected on the position sensitive detector (Colutron BVS-2) equipped with dual microchannel plates (MCPs) (40 mm) coupled with a phosphor screen (P20). Ion optics was assembled according to the design of Eppink and Parker[29] so that ion fragments with the same kinetic energy, regardless of their initial positions, can be mapped into the same position of the detector. Static electric fields on ion optics were carefully adjusted to attain the velocity mapping condition. A specific mass signal was selected by gating the front MCP using a fast high-voltage pulser (DEI, PVM4140) which gave the pulse of −500 V with the time duration in the range of 60–1000 ns depending on the experimental conditions. The time duration of the gate pulse employed in this work gave little differences to ion images. The ion images were observed through a charge-coupled-device (CCD) camera with 512×512 pixels (Hammatsu) using the center-of-gravity event-counting method. Raw images were reconstructed using the basis-set expansion (BASEX) algorithm[33] to obtain three-dimensional distributions of photofragments.

III. RESULTS AND DISCUSSION

The absorption spectrum of ICH_2CN taken in *n*-hexanes shows a broadband centered at ~ 285 nm (Fig. 2). A Gaussian-shaped structureless absorption band is one of the main characteristics of the transition to repulsive electronic states. Similar to the case of CH_3I, multiple transitions of which transition dipole moments are either parallel or perpendicular to the dissociating C–I bond axis are expected to be mixed in the broad UV absorption band of ICH_2CN in Fig. 2. Pump wavelengths of 266 and 304 nm employed in this work correspond to the blue and red shoulders of the absorption band, respectively. Considering the fact that the $(2A'', 4A')$ state lies above $3A'$ and $(1A'', 2A')$ states and the absorption band at the center wavelength is mainly due to the transition to $3A'$, it is most likely that the optical absorption at 266 nm is accompanied with the transitions to the upper
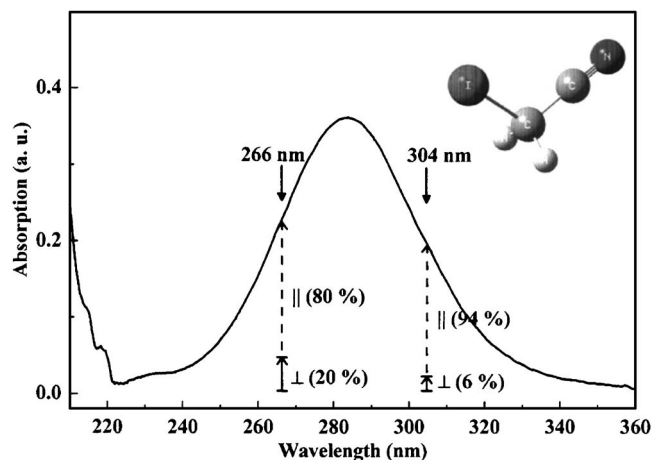
FIG. 2. UV absorption spectrum of ICH$_2$CN in n-hexane solvent. The dashed and solid lines denote the relative contributions of parallel (∥) and perpendicular (⊥) transitions, respectively, at each pump wavelength employed in this work.

lying $(2A'',4A')$ and $3A'$ states, while that at 304 nm is due to the transitions to the $3A'$ and $(1A'',2A')$ states, as schematically shown in Fig. 3. It should be noted that the transition to the $3A'$ state has a transition dipole moment parallel to the C–I bond, while the transitions to the $(2A'',4A')$ and $(1A'',2A')$ states are associated with the transition dipole moments perpendicular to the C–I bond axis.[9,34]

Raw images of I and I^* ions from the photodissociation of ICH$_2$CN at 266 and 304 nm are shown in Figs. 4 and 5, respectively. Since Newton spheres of fragments are cylindrically symmetric about the axis of the pump laser polarization, three-dimensional images of fragments could be reconstructed using the BASEX algorithm.[33] Accordingly,
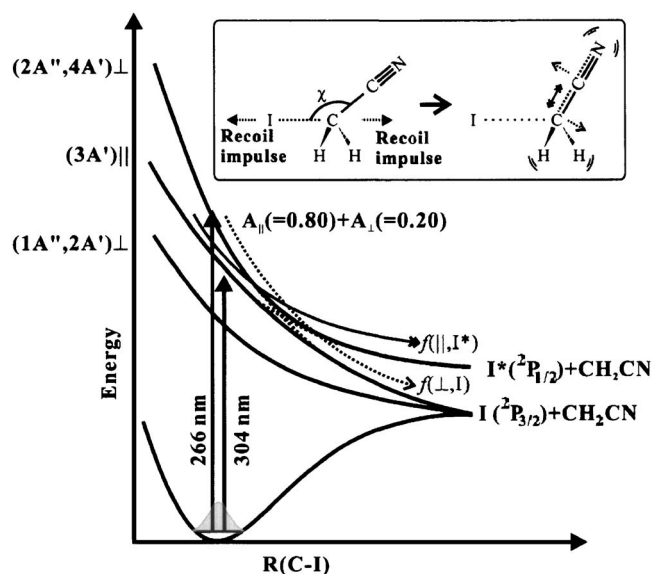

FIG. 3. Schematic diagram of potential energy curves for the photodissociation of ICH$_2$CN. The relative oscillator strengths for the parallel ($A_∥$) and perpendicular ($A_⊥$) transitions are shown for the pump wavelength of 266 nm. The nonadiabatic transition probabilities from the $(2A'',4A')$ and $3A'$ states at 266 nm are also denoted as $f(⊥,I)$, and $f(∥,I^*)$, respectively (see the text). The origin for the internal-energy excitation of the CH$_2$CN fragment induced by the recoil impulse along the C–I bond is illustrated in the inset.
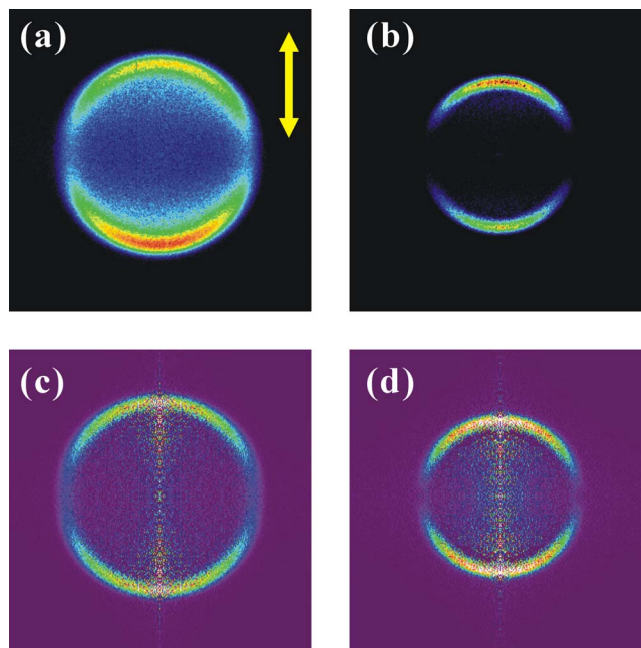

FIG. 4. Raw images of (a) I and (b) I^* in the photodissociation of ICH$_2$CN at 266 nm. Corresponding three-dimensional images of I and I^*, reconstructed by the BASEX algorithm (Ref. 33, are represented in (c) and (d), respectively. In all images, the pump laser was linearly polarized and the plane of polarization was vertical to the time-of-flight axis as shown by a vertical arrow.

translational and angular distributions of I and I^* fragments are extracted from the corresponding reconstructed images shown in Figs. 4 and 5. Absolute values of translational energies are calibrated according to the analysis of O$^+$ images from the photodissociation of O$_2$ using well-documented energetic values.[35] In this section, the energy disposal in the ICH$_2$CN photodissociation will be discussed firstly. Discus-
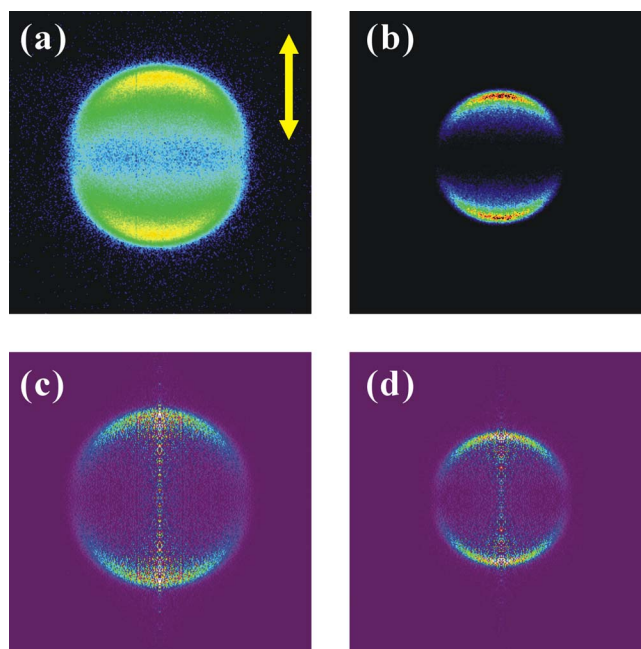

FIG. 5. Raw images of (a) I and (b) I^*, and corresponding reconstructed three-dimensional images of (c) I and (d) I^* in the photodissociation of ICH$_2$CN at 304 nm. Others are same as the caption for Fig. 4.
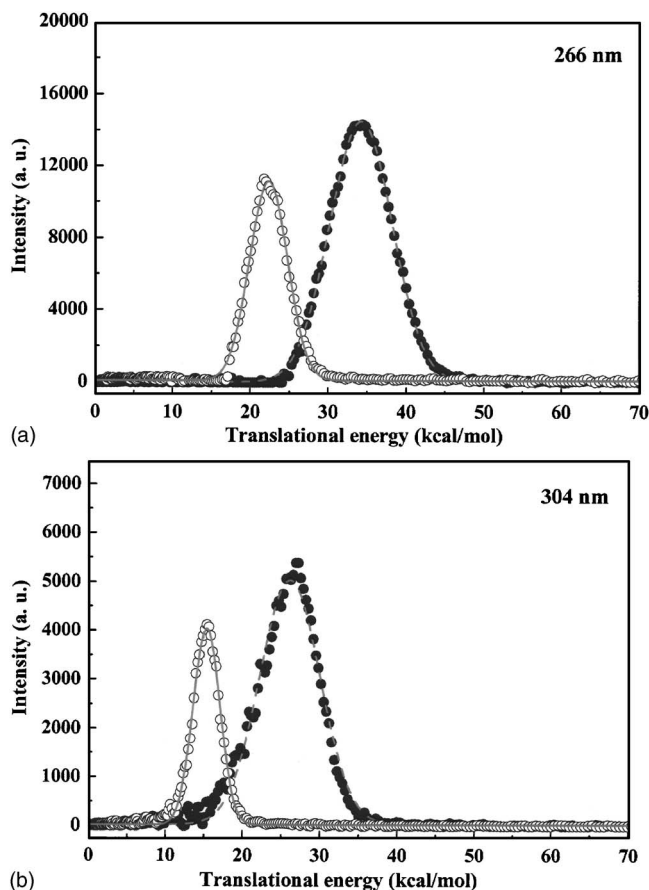
FIG. 6. Total translational energy distributions in the photodissociation of ICH$_2$CN: (a) I and I^* at 266 nm; (b) I and I^* at 304 nm. The filled or open circles represent the experimental data for the I and I^* channels, respectively. They are well reproduced by single Gaussian functions denoted by dashed or solid lines fitted for the I and I^* channels, respectively. Relative signal intensities are arbitrarily scaled.

sion on nonadiabatic dynamics and relative oscillator strengths involved in the optical transitions will be followed.

A. Translational energy distributions and energy disposal

The total translational energy distribution is easily obtained from the measured kinetic energy distributions of I or I^* fragment using the following equation:

$$E_T = \frac{m_{CH_2CN} + m_I}{m_{CH_2CN}} E_I, \quad E_T^* = \frac{E_I^*}{E_I} E_T. \qquad (1)$$

Here, E_T is the total translational energy, m_x is the mass of X, and E_I (E_I^*) is the kinetic energy of I (I^*). The resultant total

translational energy distributions for the I and I^* channels at λ_{pump}=266 and 304 nm are shown in Figs. 6(a) and 6(b), respectively. Each translational energy distribution is quite well reproduced by a single Gaussian function, indicating that the dissociation takes place promptly on repulsive excited states without complete statistical mixing among energetically accessible states. The average total translational energy of the $I+CH_2CN$ channel (I channel) $\langle E_T \rangle$ is found to be 34.9±1.0 kcal/mol, while that of the I^*+CH_2CN channel (I^* channel) $\langle E_T^* \rangle$ is 24.9±1.0 kcal/mol at the pump wavelength of 266 nm. At 304 nm, the average value of the total translation energy is found to be 25.9±1.0 and 15.9±1.0 kcal/mol for the I and I^* channels, respectively (Table I). It is interesting to note that the widths of the translational energy distributions at 266 nm are larger compared to those at 304 nm for both I and I^* channels (Fig. 6). The wider energy distribution for the translational degree of freedom means that the internal energy of the CH$_2$CN fragment is more widely distributed at 266 nm compared to that at 304 nm. Therefore, the experimental finding that the energy distribution gets wider as the pump energy increases should indicate that the dissociation is strongly coupled to nuclear motions perpendicular to the C–I bond elongation coordinate, suggesting that a significant portion of the energy may go into the internal energy of the CH$_2$CN fragment (*vide infra*).

The available energy for the I channel (E_{avl}) or I^* channel (E_{avl}^*) is obtained from the equation

$$E_{avl}(E_{avl}^*) = E_{h\nu} + E_{thermal} - D_0(-E_{el}^*), \qquad (2)$$

where $E_{thermal}$ is the initial thermal energy of ICH$_2$CN, $E_{h\nu}$ is the pump photon energy, D_0 is the C–I bond dissociation energy of ICH$_2$CN, and E_{el}^* is the electronic energy of I^* with respect to that of the ground state I. $E_{thermal}$ is very small in the molecular beam (∼5 K) and assumed to be zero. The E_{el}^* value is exactly known to be 21.74 kcal/mol.[36] D_0 is deduced from experimentally measured heats of formation of reactant and products according to the thermochemical cycle as follows:

$$D_0 = \Delta H_f^0(I,0\ K) + \Delta H_f^0(CH_2CN,0\ K) - \Delta H_f^0(ICH_2CN,0\ K). \qquad (3)$$

The heats of formation have recently been reported by Lafleur *et al.*[32] to give $\Delta H_f^0(I,0\ K)$=25.63 kcal/mol, $\Delta H_f^0(CH_2CN,0\ K)$=60.99±1.0 kcal/mol, and $\Delta H_f^0(ICH_2CN,0\ K)$=42.95 kcal/mol. Accordingly, the C–I bond dissociation energy of ICH$_2$CN is estimated to be 43.67±1.0 kcal/mol. This value is ∼22% smaller than the

TABLE I. The energy partitioning of I and I^* in the photodissociation of ICH$_2$CN at 266 and 304 nm. The bond dissociation energy D_0 is 43.67±1.0 kcal/mol (unit: kcal/mol).

		E_{avl}	$\bar{E}_T$	f_T	f_T^{soft}	f_T^{rigid}
266 nm	I	63.89±1.0	34.9±1.0	0.55±0.03	0.36	0.54
	I^*	42.14±1.0	24.9±1.0	0.59±0.04	0.36	0.54
304 nm	I	50.26±1.0	25.9±1.0	0.52±0.03	0.36	0.54
	I^*	28.51±1.0	15.9±1.0	0.55±0.05	0.36	0.54

C–I bond dissociation energy of 55.59 kcal/mol of CH$_3$I,[10] indicating that the CN moiety as an electron-withdrawing group not only causes a red spectral shift in the absorption but also weakens the adjacent C–I bond significantly. For ICH$_2$CN, $E_{avl}(E_{avl}^*)$ is, therefore, estimated to be 63.89 (42.14) or 50.26 (28.51) kcal/mol at 266 and 304 nm, respectively. The fraction of the translational energy, defined as $f_T = \langle E_T \rangle / E_{avl}$ or $f_T^* = \langle E_T^* \rangle / E_{avl}^*$, is determined at both pump energies and listed in Table I. It is found that $f_T = 0.55$ (0.52) and $f_T^* = 0.59$ (0.55) at 266 (304) nm. Although there are some differences in the f_T values for different channels at different pump energies, all the fractions of the translational energy fall in the range of 0.52–0.59.

A simple impulsive model,[37] where all the available energy is assumed to be concentrated on the dissociating C–I bond as an instantaneous impulse, predicts the translational fraction to be 0.36 according to the following equation:

$$E_T = \frac{\mu_{C-I}}{\mu_{ICH_2CN}} E_{avl}. \tag{4}$$

Here, μ_{C-I} is a reduced mass of the departing C and I atoms, while μ_{I-CH_2CN} is the reduced mass of I and CH$_2$CN fragments. This model predicts the smaller translational fraction of the available energy compared to the experiment, suggesting that bond dissociation dynamics of ICH$_2$CN may be rather more complicated than a simple diatomiclike bond rupture. A modified impulsive model,[37,38] in which all the internal energy is assumed to go into the rotational energy of fragments (E_{rot}), is also tested. This model should be suitable to the case of photodissociation of triatomiclike systems. Here, under the assumption that the C–CN bond is extremely stiff, the translational fraction is calculated according to the modified impulsive model,

$$E_{rot} = \left(1 + \frac{I_{CH_2CN}}{\mu_{I-CH_2CN} r_{c.m.}^2 \sin^2 \chi} \right)^{-1} E_{avl}, \tag{5}$$

$$E_T = E_{avl} - E_{rot}, \tag{6}$$

where I_{CH_2CN} denotes the moment of inertia of CH$_2$CN calculated for the rotational motion about the axis perpendicular to the dissociating I–C–CN plane, $r_{c.m.}$ is the distance between the center of mass of CH$_2$CN and the dissociating carbon atom, and χ is the angle between the C–I bond axis and a line connecting the center of mass of CH$_2$CN and dissociating carbon atom. The minimum energy structure of ICH$_2$CN calculated by *ab initio* calculation (Hartree-Fock, 6-311G** basis set) is used for the evaluation of the fraction to give $f_T = 0.54$. This value is amazingly in good agreement with the experiment (Table I). Even though the assumption for the stiffness of the C–CN bond in the modified impulsive model is quite less likely, the instantaneous kicking along the C–I bond may give the instantaneous rotational excitation of the CH$_2$CN moiety of dissociating ICH$_2$CN which may lead to excitations of associated vibrational modes such as C–CN bending of the CH$_2$CN fragment when it is completely separated out. At the asymptotic limit, an unpaired electron in the $2p$ orbital of the departing carbon atom should be involved in the formation of a conjugated π bond between CH$_2$ and CN moieties. Actually, it had been found from a previous microwave study[39] that the CH$_2$CN radical has the longer C≡N (1.192 Å) and shorter C–C (1.368 Å) bonds compared to C≡N (1.156 Å) and C–C (1.457 Å) bonds of CH$_3$CN.[39–43] Therefore, it is possible that as the C–I bond elongates, a rapid electron rearrangement leading to the shortening of the C–CN bond might occur, as shown in Fig. 3. In this case, the reaction coordinate is strongly coupled to nuclear motions perpendicular to the reaction coordinate, and relatively large fraction of the available energy may go into the internal energy of the CH$_2$CN fragment. The experimental finding that the translational energy distribution is wider at 266 nm compared to that at 304 nm is also consistent with above.

B. Nonadiabatic dynamics

The images in Figs. 4 and 5 show the anisotropic spatial distribution of the I and I^* fragments, reflecting the orientation of associated transition dipole moments with respect to the pump polarization. The anisotropy parameter (β), defined as follows, is often used for the extent of anisotropy in the spatial distribution:

$$I(\theta) \propto (1 + \beta P_2(\cos \theta)). \tag{7}$$

Here $I(\theta)$ is the ion signal intensity as a function of the angle θ between the recoil velocity vector of fragments and the pump polarization axis. $P_2(\cos \theta)$ is the second order Legendre polynomial. For a diatomic molecule, β varies from 2 for parallel to -1 for perpendicular transitions. The β values averaged over the range of full widths at half maximum (FWHM's) of translational energy distributions are listed in Table II. The measured anisotropy parameters extracted from the reconstructed images give $\beta(I) = 1.10 \pm 0.05$ (1.70 ± 0.05) and $\beta(I^*) = 1.60 \pm 0.05$ (1.90 ± 0.05) at 266 (304) nm. As stated earlier, the absorption at 304 nm is due to the transitions to the ($1A''$, $2A'$) and $3A'$ states. While the $3A'$ state is diabatically (or adiabatically) correlated to the I^* channel (or I channel), the lower lying ($1A''$, $2A'$) state is correlated only to the I channel. Therefore, the β value obtained for the I^* channel at 304 nm should represent the effective anisotropy parameter for the parallel transition of ICH$_2$CN, giving $\beta_\parallel^{eff} = 1.90$. Thereafter, the effective anisotropy parameter for the perpendicular transition of ICH$_2$CN is estimated to be $\beta_\perp^{eff} = -0.95$ from a simple formula of $\beta_\perp^{eff} = -0.5 \beta_\parallel^{eff}$. The measured anisotropy parameters in Table II reflect both the extent of mixing of the parallel/perpendicular transitions and nonadiabatic transitions along the reaction coordinate. In order to disentangle the complex dynamics involved, we have measured the absolute I^*/I branching ratios at 266 and 304 nm. The ratio of ion signal intensities of I^* and I from the ICH$_2$CN photodissociation is measured and scaled to give the relative quantum yield of I^*; $\Phi_I^* = 0.42 \pm 0.02$ or 0.12 ± 0.03 at 266 and 304 nm, respectively. It should be noted that the scaling factor is determined from a controlled experiment on CH$_3$I. Namely, under identical experimental conditions, the I^*/I ion intensity ratio from the CH$_3$I photodissociation has been measured and scaled to be matched with a well-established I^*/I branching ratio reported in Refs.

TABLE II. The anisotropy parameters and relative quantum yields of I and I^* in the photodissociation of ICH$_2$CN at 266 and 304 nm. Just for the comparison, the previously reported values of β and Φ for the CH$_3$I dissociation at the same pump wavelengths are shown together.

		β		Φ	
		ICH$_2$CN	CH$_3$I	ICH$_2$CN	CH$_3$I
266 nm	I	1.10 ± 0.05	1.7 ± 0.1[a] 1.8 ± 0.1[c]	0.58 ± 0.03	0.27[b]
	I^*	1.60 ± 0.05	1.8 ± 0.1[a] 1.9 ± 0.1[c]	0.42 ± 0.02	0.73 ± 0.04[b]
304 nm	I	1.70 ± 0.06	1.6 ± 0.1[a] 1.5 ± 0.1	0.88 ± 0.03	0.80[a,d]
	I^*	1.90 ± 0.06	1.8 ± 0.1[a] 1.9 ± 0.1	0.12 ± 0.03	0.20[a,d]

[a]References 20 and 27.
[b]References 1 and 18.
[c]Reference 26.
[d]Reference 6.

1, 6, and 27, giving the corresponding scaling factor which is used for ICH$_2$CN. The I^*/I branching ratios of ICH$_2$CN is consequently determined to be 0.724 or 0.136 at 266 and 304 nm, respectively.

From measured anisotropy parameters and branching ratios at each pump wavelength, it is now possible to get the quantitative information about relative oscillator strengths and nonadiabatic transitions. If it is assumed that the optical absorption at 266 nm is associated with $3A'$ and $(2A'', 4A')$ states, then the measured branching ratio and anisotropy parameters can be expressed as follows:

$$\frac{\Phi_I^*}{\Phi_I} = \frac{A_\parallel f(\parallel, I^*) + A_\perp f(\perp, I^*)}{A_\parallel f(\parallel, I) + A_\perp f(\perp, I)}, \tag{8}$$

$$\beta(I^*) = \frac{A_\parallel f(\parallel, I^*)\beta_\parallel^{\text{eff}} + A_\perp f(\perp, I^*)\beta_\perp^{\text{eff}}}{A_\parallel f(\parallel, I^*) + A_\perp f(\perp, I^*)}, \tag{9}$$

$$\beta(I) = \frac{A_\parallel f(\parallel, I)\beta_\parallel^{\text{eff}} + A_\perp f(\perp, I)\beta_\perp^{\text{eff}}}{A_\parallel f(\parallel, I) + A_\perp f(\perp, I)}. \tag{10}$$

Here, $A_\parallel$ or $A_\perp$ represents a relative oscillator strength for the transition to the $3A'$ and $(2A'', 4A')$ states, respectively, with $A_\parallel + A_\perp = 1$. The value of $f(\parallel, I)$ or $f(\parallel, I^*)$ represents a fraction of the wave packet prepared by the parallel transition going

into the I or I^* channel, respectively. Similarly, $f(\perp, I)$ or $f(\perp, I^*)$ represents a faction into the I and I^* channels, respectively, from the wave packet prepared by the perpendicular transition. It is defined that $f(\parallel, I) + f(\parallel, I^*) = f(\perp, I) + f(\perp, I^*) = 1$. It is useful to note that $f(\parallel, I)$ and $f(\perp, I^*)$ represent the probabilities for the wave packet to follow their adiabatic reaction paths, while $f(\parallel, I^*)$ and $f(\perp, I)$ are the probabilities for the wave packet to move on diabatic potential energy surfaces. Using the above equations with the measured experimental values, one gets the numerical values for all the variables: $A_\parallel = 0.80$, $A_\perp = 0.20$, $f(\parallel, I) = 0.53$, $f(\parallel, I^*) = 0.47$, $f(\perp, I) = 0.79$, and $f(\perp, I^*) = 0.21$, (Table III). These values give a very clear picture for the relative oscillator strengths and complex nonadiabatic transition dynamics along the reaction coordinate, as depicted in Fig. 3. Namely, at the pump wavelength of 266 nm, the relative oscillator strengths of the parallel $(3A')$ and perpendicular $(2A'', 4A')$ transitions are 0.80 and 0.20, respectively. A wave packet prepared on the $3A'$ state proceeds adiabatically to give the I fragment with a probability of 53%, while it undergoes a nonadiabatic transition to give I^* with a chance of 47%. Meanwhile, the wave packet on the $(2A'', 4A')$ state proceeds on the adiabatic surface with a 21% probability and it under-

TABLE III. Relative oscillator strengths and fractions of the wave packets associated with possible dissociation pathways calculated by Eqs. (8)–(12).

	$A_\parallel$	$A_\perp$	$f(\parallel, I)$,	$f(\parallel, I^*)$[a]	$f(\perp, I)$[b]	$f(\perp, I^*)$
266 nm	0.80 ± 0.09	0.20 ± 0.09	0.53 ± 0.06	0.47 ± 0.06	0.79 ± 0.05	0.21 ± 0.05
304 nm	0.94 ± 0.01	0.06 ± 0.01	0.87 ± 0.07	0.13 ± 0.07	$\cdots$	$\cdots$

[a]The nonadiabatic transition probability from the initially prepared $3A'$ state to give I^*.
[b]The nonadiabatic transition probability from the initially prepared $(2A'', 4A')$ state to give I.

goes a nonadiabatic transition to give the I fragment with a 79% chance.

Similar treatment can be applied to the case of the photodissociation at 304 nm. Here the optical absorption is ascribed to the transitions to the $3A'$ and $(1A'',2A')$ states, where the former and latter are parallel and perpendicular transitions, respectively. Since the $(1A'',2A')$ state is correlated only to the I channel, the expressions for the branching ratio and anisotropy parameters become much simpler,

$$\frac{\Phi_I^*}{\Phi_I} = \frac{A_\parallel f(\parallel,I^*)}{A_\parallel f(\parallel,I) + A_\perp}, \tag{11}$$

$$\beta(I) = \frac{A_\parallel f(\parallel,I^*)\beta_\parallel^{\text{eff}} + A_\perp \beta_\perp^{\text{eff}}}{A_\parallel f(\parallel,I) + A_\perp}. \tag{12}$$

At 304 nm, it is found that $A_\parallel = 0.94$, $A_\perp = 0.06$, $f(\parallel,I) = 0.87$, and $f(\parallel,I^*) = 0.13$, as listed in Table III. A contribution of the perpendicular transition to the optical absorption at 304 nm is found to be ∼6%. The nonadiabatic transition probability of the wave packet on the $3A'$ state at 304 nm (0.13) is much smaller than that found at 266 nm (0.79) (Fig. 2).

The Landau-Zener probability (P) for a transition from one adiabatic surface to another[44] is given by

$$P = \exp\left(-\frac{\xi}{v_c}\right) = \exp\left(\frac{-4\pi^2 V_{12}^2}{h|\Delta F|v_c}\right), \tag{13}$$

where ξ is the Landau-Zener adiabaticity parameter, v_c is the velocity between photofragments passing through a nonadiabatic transition point, V_{12} is the adiabatic curve splitting, and $|\Delta F|$ is the difference in slopes of two diabatic curves at the nonadiabatic transition point. From above, the nonadiabatic transition probability from the upper lying $(2A'',4A')$ state is much larger than that from the $3A'$ state for the wave packet prepared at 266 nm. The shapes of two potential energy surfaces near the nonadiabatic transition point are supposed to be same for both directions of transition. Thus the steeper potential energy surface for the wave packet motion on the upper $(2A'',4A')$ electronic state might be responsible for the higher nonadiabatic transition probability. It is also interesting to note that the nonadiabatic transition probability of 0.47 from the $3A'$ state in the ICH₂CN dissociation at 266 nm is quite different from the nonadiabatic transition probability of 0.68–0.75 found in the CH₃I dissociation at the same wavelength.[19,26] This discrepancy indicates that the simple one-dimensional Landau-Zener model is inappropriate for polyatomic molecules and/or that V_{12} at the nonadiabatic transition point may be larger in the case of ICH₂CN compared to that of CH₃I. Theoretical calculations would be desirable for the explanation of this interesting difference of two systems. The smaller nonadiabatic transition probability of the wave packet on the $3A'$ state at 304 nm (0.13) compared to that at 266 nm (0.79) should be due to the fact that the wave packet motion at the nonadiabatic transition point at 304 nm is much slower than that at 266 nm due to the relatively smaller available energy at 304 nm. The nonadiabatic transition probabilities at various occasions are plotted versus the square roots of total kinetic energies, assuming that the relative velocity of fragments at the nonadiabatic
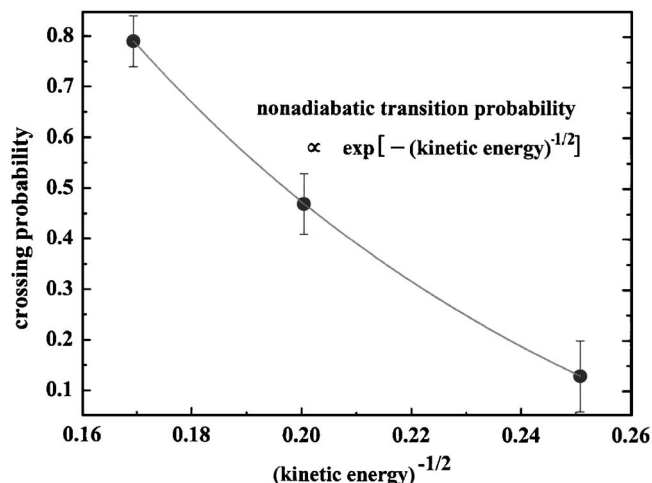

FIG. 7. The nonadiabatic transition probability plotted vs (kinetic energy)$^{-1/2}$. The experimental results (filled circles) show an exponential decay (a solid line), which is consistent with the prediction by the Landau-Zener model (see the text).

transition point is given by the total kinetic energy of fragments at the asymptote (Fig. 7). Interestingly, the nonadiabatic transition probability shows an exponential decay as (kinetic energy)$^{1/2}$ gets smaller, which is consistent with the prediction from the Landau-Zener model. Even though the Landau-Zener model is based on the simplified one-dimensional semiclassical description for the nonadiabatic transition probability, the concept regarding to the nonadiabatic transition behavior as a function of the nuclear velocity along the reaction coordinate seems to work fine for the ICH₂CN dissociation. The nonadiabatic transition between electronic states of polyatomic molecules is a challenging subject from both experimental and theoretical points of view. Our experimental results on the nonadiabatic transition in the ICH₂CN dissociation should be helpful for a better understanding of complex dynamics occurring in polyatomic molecules.

IV. SUMMARY AND CONCLUSION

In this work, we have investigated photodissociation dynamics of ICH₂CN at 266 and 304 nm using a velocity-map ion imaging method. The C–I bond dissociation is prompt, and thus large anisotropy has been observed. Because of the electron-withdrawing nature of the CN moiety, the C–I bond dissociation energy of ICH₂CN turns out to be smaller than that of other alkyl iodides such as CH₃I. A significant portion (∼45%) of the available energy goes into the internal energy of the CH₂CN fragment, indicating that the reaction coordinate is coupled to nuclear motions perpendicular to the C–I elongation axis. This relatively large fraction into internal energy should be closely related to the structural change of the CH₂CN moiety as the C–I bond elongates. The relative oscillator strengths of the parallel and perpendicular transitions mixed at 266 and 304 nm are estimated from the anisotropy parameters and I^*/I branching ratios. The nonadiabatic transition probabilities from individual potential energy surfaces are definitely determined to give the detailed picture of nonadiabatic dynamics occurring in the ICH₂CN photo-

dissociation. Nonadiabatic dynamics could be conceptually explained using a simple Landau-Zener model. The more quantitative explanation would require the more evolved theoretical formulation for nonadiabatic dynamics.

ACKNOWLEDGMENTS

[1] S. J. Riley and K. R. Wilson, Faraday Discuss. Chem. Soc. **53**, 132 (1972).

[2] R. K. Sparks, K. Shobatake, L. R. Carlson, and Y. T. Lee, J. Chem. Phys. **75**, 3838 (1981).

[3] D. M. Szaflarski, R. van den Berg, and M. A. El-Sayed, J. Phys. Chem. **93**, 6700 (1989).

[4] F. G. Godwin, P. A. Gorry, P. M. Hughes, D. Raybone, T. M. Watkinson, and J. C. Whitehead, Chem. Phys. Lett. **135**, 163 (1987).

[5] D. W. Chandler, J. W. Thoman, Jr., M. H. M. Janssen, and D. H. Parker, Chem. Phys. Lett. **156**, 151 (1989).

[6] W. K. Kang, K. W. Jung, D.-C. Kim, and K.-H. Jung, J. Chem. Phys. **104**, 5815 (1996).

[7] S. Uma and P. K. Das, J. Chem. Phys. **104**, 4470 (1996).

[8] Y. J. Jung, Y. S. Kim, W. K. Kang, and K. H. Jung, J. Chem. Phys. **107**, 7187 (1997).

[9] W. S. McGivern, R. Li, P. Zou, and S. W. North, J. Chem. Phys. **111**, 5771 (1999).

[10] A. T. J. B. Eppink and D. H. Parker, J. Chem. Phys. **110**, 832 (1999).

[11] K. Kavita and P. K. Das, J. Chem. Phys. **112**, 8426 (2000).

[12] P. Zou, W. S. McGivern, and S. W. North, Phys. Chem. Chem. Phys. **2**, 3785 (2000).

[13] F. Aguirre and S. T. Pratt, J. Chem. Phys. **118**, 1175 (2003).

[14] R. S. Mulliken, J. Chem. Phys. **8**, 382 (1940).

[15] A. Gedanken and M. D. Rowe, Chem. Phys. Lett. **34**, 39 (1975).

[16] H. W. Hermann and S. R. Leone, J. Chem. Phys. **76**, 4766 (1982).

[17] G. N. A. van Veen, T. Baller, A. E. de Vries, and N. J. A. van Veen, Chem. Phys. **87**, 405 (1984).

[18] W. P. Hess, S. J. Kohler, H. K. Haugen, and S. R. Leone, J. Chem. Phys. **84**, 2143 (1986).

[19] M. Shapiro, J. Phys. Chem. **90**, 3644 (1986).

[20] R. O. Loo, H. P. Haerri, G. E. Hall, and P. L. Houston, J. Chem. Phys. **90**, 4222 (1989).

[21] I. Powis and J. F. Black, J. Phys. Chem. **93**, 2461 (1989).

[22] H. Guo and G. C. Schatz, J. Chem. Phys. **93**, 393 (1990).

[23] K. Q. Lao, M. D. Person, P. Xayariboun, and L. J. Butler, J. Chem. Phys. **92**, 838 (1990).

[24] Y. Amatatsu and K. Morokuma, J. Chem. Phys. **94**, 4858 (1991).

[25] M. D. Person, P. W. Kash, and L. J. Butler, J. Chem. Phys. **94**, 2557 (1991).

[26] J. A. Syage, J. Chem. Phys. **105**, 1007 (1996).

[27] A. T. J. B. Eppink and D. H. Parker, J. Chem. Phys. **109**, 4758 (1998).

[28] M. Dzvonik, S. Yang, and R. Bersohn, J. Chem. Phys. **61**, 4408 (1974).

[29] A. T. J. B. Eppink and D. H. Parker, Rev. Sci. Instrum. **68**, 3477 (1997).

[30] M. S. Park, T. K. Kim, S.-H. Lee, K.-H. Jung, H.-R. Volpp, and J. Wolfrum, J. Phys. Chem. A **105**, 5606 (2001).

[31] K.-S. Lee, K. W. Lee, T. K. Kim, R. Ryoo, and K.-H. Jung, J. Chem. Phys. **122**, 034308 (2005).

[32] R. D. Lafleur, B. Szatary, and T. Baer, J. Phys. Chem. A **104**, 1450 (2000).

[33] V. Dribinski, A. Ossadtchi, V. A. Mandelshtam, and H. Reisler, Rev. Sci. Instrum. **73**, 2634 (2002).

[34] K. W. Lee, Y.-J. Jee, and K.-H. Jung, J. Chem. Phys. **116**, 4490 (2002).

[35] D. H. Parker and A. T. J. B. Eppink, J. Chem. Phys. **107**, 2357 (1997).

[36] L. Minnhagen, Ark. Fys. **21**, 415 (1962).

[37] G. E. Busch and K. R. Wilson, J. Chem. Phys. **56**, 3626 (1972).

[38] G. E. Busch and K. R. Wilson, J. Chem. Phys. **56**, 3655 (1972).

[39] *Structure Data of Free Polyatomic Molecules*, edited by K. Kuchitsu, Landolt-Börnstein, New Series, Group 2, Vol. 23, Molecules and Radicals (Springer-Verlag, Heidelberg, 1995).

[40] J. L. Holmes, F. P. Lossing, and P. M. Mayer, Chem. Phys. Lett. **212**, 134 (1993).

[41] S. Saito and S. Yamamoto, J. Chem. Phys. **107**, 1732 (1997).

[42] P. M. Mayer, M. S. Taylor, M. W. Wong, and L. Radom, J. Phys. Chem. A **102**, 7074 (1998).

[43] F. G. Bordwell, X.-M. Zhang, and M. S. Alnajjar, J. Am. Chem. Soc. **114**, 7623 (1992).

[44] L. D. Landau and E. M. Lifshitz, *Quantum Mechanics*, 3rd ed. (Pergamon, New York, 1977).